Two-dimensional numerical investigations of small-amplitude disturbances in a boundary layer at Ma=4.8: Compression corner versus impinging shock wave

Alessandro Pagella, Andreas Babucke, and Ulrich Rist
Institut für Aerodynamik und Gasdynamik, Universität Stuttgart, 70550 Stuttgart, Germany

(Received 15 April 2003; accepted 17 March 2004; published online 18 May 2004)

Two-dimensional direct numerical simulations and linear stability theory investigations have been carried out for a compression ramp at Ma=4.8 and compared to earlier results of a laminar boundary layer with impinging shock wave. The inflow parameters in both flows were identical; the ramp angle of the compression corner was chosen to cause a separation bubble, which has exactly the same length compared to the case with impinging shock. It turned out, that the two cases are almost identical for the base flow properties. This is in accordance with similarity assumptions, e.g., free interaction theory, which for smaller Reynolds numbers states, that the boundary layer should be independent of the sort of shock-boundary layer interaction. However, linear stability theory results differ near the corner and the impinging shock, respectively. Direct numerical simulations of small-amplitude disturbances, which were introduced into the laminar boundary layer, also behave in a very similar way. Amplitude distributions exhibit the same characteristics. The according distributions of the ramp flow have slightly larger amplitudes than the case with impinging shock.
 [DOI: 10.1063/1.1738414]

I. INTRODUCTION

Shock boundary layer interaction is one major area of concern in technical applications at trans-, super-, and hypersonic speeds. As discussed in many publications over the last decades, it can result in high aerodynamic loads, engine inlet performance loss and increase of drag, to name only a few examples. The base flow properties of shock-boundary layer interactions for simple geometries, such as an impinging shock wave on a flat-plate boundary layer, a forward or rearward facing step and the compression ramp problem have been thoroughly explained in the many publications. A good summary can be found in Ref. 1. For a compression ramp the following physical phenomena occur: The change in direction of the wall due to the ramp forces the boundary layer to follow the contour, which causes a pressure gradient yielding the boundary layer thickness to increase. Depending on such parameters like the ramp angle, the Reynolds number, the wall temperature conditions, and the boundary layer thickness, a complicated system of compression waves occurs. Provided the ramp angle is large enough, the boundary layer separates. Compression waves form upstream from the corner, which is caused by an initial turn of the flow at separation. Well outside the boundary layer, those coalesce to the separation shock. At reattachment, additional compression waves are present, which merge with the separation shock. Another possible scenario is the formation of a reattachment shock before the compression waves reach the separation shock. The two shocks will then meet at the so-called triple or bifurcation point. Although the base flow properties have been intensively studied, much less is known about the transitional behavior of such flows with shock-boundary layer interaction. In one of our recent papers we discussed the transitional behavior for a Ma=4.8 boundary layer with impinging shock and small amplitude disturbances.[2] In the present paper, we will compare the results obtained in Ref. 2 with a compression ramp flow. The flow parameters of the ramp flow calculations correspond to the parameters used in Ref. 2. The ramp angle was chosen to induce a separation bubble which has the same length at the wall compared to the separation bubble in the case with impinging shock in Ref. 2. Early experimental results, such as experiments referred to in Ref. 1 and, more recently in Ref. 3 indicated that flows with shock-boundary layer interaction do behave in a similar manner in major parts, independent of the cause of separation (impinging shock, ramp or step). This led to the derivation of some correlation laws, which are known as the free interaction concept.[1] These similarity assumptions were the motivation for the present investigations. We wanted to study, whether this also holds for controlled, unsteady disturbance behavior, which, if the answer is yes would be helpful because according results obtained for the flat plate[2] could be applied to the compression corner in a quantitative manner and vice versa. However, related publications are not known to the authors. Within this paper, a two-dimensional compression-ramp boundary layer with small-amplitude disturbances is investigated numerically both with compressible linear stability theory[4] and direct numerical simulation.

II. NUMERICAL SCHEME

A. Governing equations, disrcretization, initial and boundary conditions

Linear stability theory investigations are based on the scheme developed by Mack[4] using local velocity and temperature profiles extracted from the direct numerical simula-

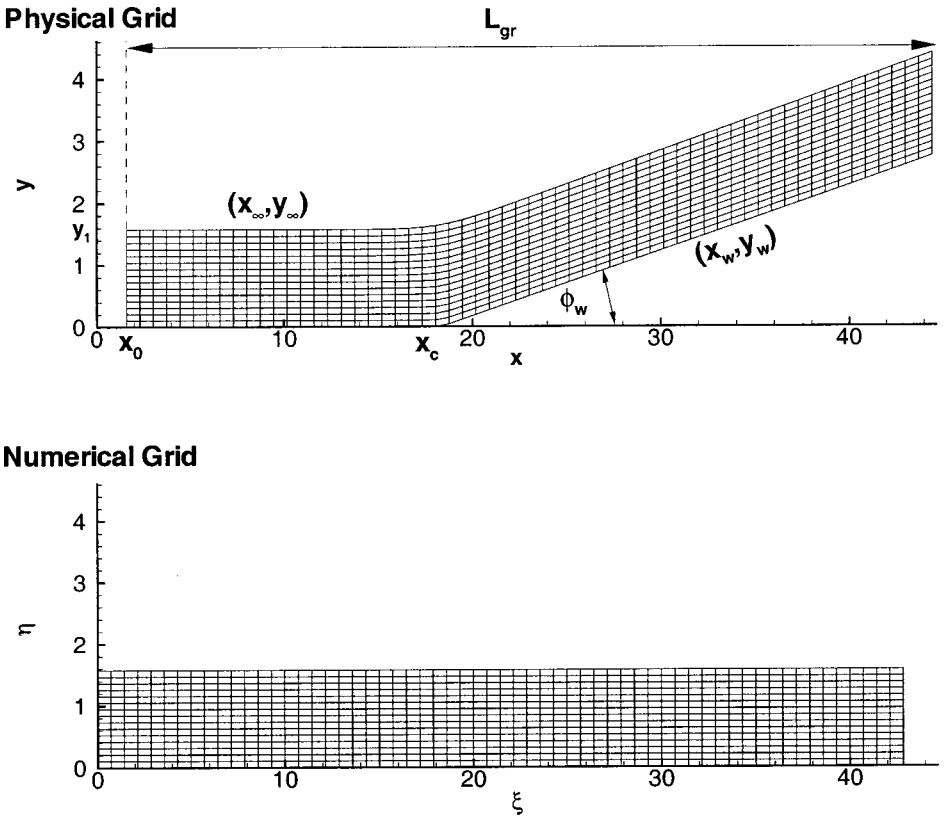

FIG. 1. Physical (upper figure) and numerical grid (lower figure) typically used in our simulations.

tion of the base flow calculation.[2] The numerical scheme used for the direct numerical simulation is based on the complete two-dimensional Navier–Stokes equations in conservative formulation. The description of the numerical scheme in this paper will be very limited regarding features already presented earlier.[2,5]

For the simulations with a compression corner, a boundary-fitted grid in the physical $x-y$ space is needed to properly represent the geometry, which has to be mapped onto an equally spaced and equidistant grid in the numerical $\xi-\eta$ space (see Fig. 1). This has been achieved by an appropriate transformation of the Navier–Stokes equations, according to the scheme presented in Ref. 6. The derivatives in the streamwise direction now become

$$\frac{\partial}{\partial x}=\frac{1}{J}\left[\left(\frac{\partial}{\partial \xi}\right)\left(\frac{\partial y}{\partial \eta}\right)-\left(\frac{\partial}{\partial \eta}\right)\left(\frac{\partial y}{\partial \xi}\right)\right], \tag{1}$$

and in the wall-normal direction

$$\frac{\partial}{\partial y}=\frac{1}{J}\left[\left(\frac{\partial}{\partial \eta}\right)\left(\frac{\partial x}{\partial \xi}\right)-\left(\frac{\partial}{\partial \xi}\right)\left(\frac{\partial x}{\partial \eta}\right)\right]. \tag{2}$$

Second derivatives are implemented by applying the first derivative twice. The transformed flux vectors are then

$$\mathbf{F_t}=\mathbf{F}\frac{\partial y}{\partial \eta}+\mathbf{G}\frac{\partial x}{\partial \eta} \tag{3}$$

in streamwise direction and

$$\mathbf{G_t}=-\mathbf{F}\frac{\partial y}{\partial \xi}+\mathbf{G}\frac{\partial x}{\partial \xi} \tag{4}$$

in wall-normal direction, respectively. **F** and **G** are the flux vectors of the original, untransformed Navier–Stokes equations. The transformed, conservative solution vector is given by

$$\mathbf{Q_t}=J\cdot\mathbf{Q} \tag{5}$$

with **Q** as the solution vector of the untransformed Navier–Stokes equations, where

$$J=\frac{\partial x}{\partial \xi}\cdot\frac{\partial y}{\partial \eta}-\frac{\partial y}{\partial \xi}\cdot\frac{\partial x}{\partial \eta} \tag{6}$$

is the determinant of the Jacobi matrix. The transformed Navier–Stokes equations in numerical space are then

$$\frac{\partial \mathbf{Q_t}}{\partial t}+\frac{\partial \mathbf{F_t}}{\partial \xi}+\frac{\partial \mathbf{G_t}}{\partial \eta}=\mathbf{0}. \tag{7}$$

High-order compact finite differences in split-type formulation are used for streamwise derivatives, while in wall-normal direction high-order finite differences are applied for convective and central differences for viscous terms. Time integration is performed with a standard fourth-order accurate Runge–Kutta scheme. In contrast to the simulations with impinging shock in Ref. 2 it was not necessary to apply a filter[7] in the ramp case. Because a shock wave impinging on the boundary layer is not present, gradients of the flow quantities in the streamwise direction are not as high as in Ref. 2. The inflow boundary variables and the wall temperature are held constant. In the untransformed scheme, the wall pres-

TABLE I. Relevant grid parameters used in simulations.

Case	$M\times N$	Δy	Δx
Standard	301×1201	0.005 25	0.035 6999
Finer Δx	301×2401	0.005 25	0.017 849 95
Finer Δy	601×1201	0.002 625	0.035 6999
Higher domain	601×1201	0.005 25	0.035 6999
Impinging shock, $\sigma=14°$	301× 801	0.005 25	0.035 6999

sure is calculated from the v-momentum equation.[8] In the transformed case, derivatives in both the ξ and η direction are present in the v-momentum equation,

$$J\frac{\partial}{\partial t}\{\rho v\}+\frac{\partial}{\partial \xi}\left\{\frac{\partial y}{\partial \eta}(\rho uv-\tau_{xy})+\frac{\partial x}{\partial \eta}(\rho v^2+p-\tau_{yy})\right\}+\frac{\partial}{\partial \eta}\left\{-\frac{\partial y}{\partial \xi}(\rho uv-\tau_{xy})+\frac{\partial x}{\partial \xi}(\rho v^2+p-\tau_{yy})\right\}=0. \quad (8)$$

In the general case, the wall pressure has to be calculated implicitly, because derivatives in both the ξ and η direction are present, as it can be seen in Eq. (8). However, a grid with the metric coefficient $\partial x/\partial \eta=0$ simplifies the wall-pressure calculation, so it can be calculated in an analogous manner as in the untransformed case. Therefore, the grids used for calculations presented within this paper are generated accordingly.

The boundary layer is perturbed by simulated blowing and suction at a disturbance strip on the wall. At the outflow boundary, flow variables are calculated with the Navier–Stokes equations neglecting second derivatives. First derivatives are obtained by a second-order backward difference. At the beginning of the simulation, a laminar flow obtained by the compressible boundary layer equations is specified within the whole integration domain. Velocities, energy, viscosity, density, and the temperature are normalized with their respective free stream values, the pressure and energy by the dynamic pressure $\rho_\infty^* u_\infty^{*2}$, specific heat coefficients c_v and c_p with u_∞^{*2}/T_∞^*. Dimensional variables are labeled with an asterisk. In the streamwise direction, the square root of the local Reynolds number $R_x=\sqrt{x\,\mathrm{Re}}$ is used as a measure for the streamwise location on the body, with the global Reynolds number $\mathrm{Re}=100\,000$. From this global Reynolds number $\mathrm{Re}=\rho_\infty^* u_\infty^* L/\mu_\infty^*$ a length scale L is obtained. L normalizes lengths such as the streamwise and wall-normal coordinates $x=x^*/L$ and $y=y^*/L$. For temperatures above the Sutherland temperature viscosity $\mu=\mu^*/\mu_\infty^*$ is calculated by Sutherland's law, below the relation $\mu^*/\mu_\infty^*=T^*/T_\infty^*$ is used.

B. Computation of the grid

Our formulation of the grid is based on the analytical function presented in Ref. 9. We have

$$y=a\cdot\left(x+\frac{\ln[\cosh(c(x-x_c))]}{c}-\frac{\ln[\cosh(c\cdot x_c)]}{c}\right)+Y, \quad (9)$$

with $Y=0$ at the wall and $Y=y_1$ for $y=\infty$ at the inflow boundary. x_c is the streamwise coordinate of the corner, and c describes the magnitude of the radius at the corner and at the free stream, respectively. For a ramp angle ϕ,

$$\tan(\phi)=\frac{y_{(x=L_{gr})}}{L_{gr}-x_c}, \quad (10)$$

a is given by the relation

$$a=-\frac{\tan(\phi)c[L_{gr}-x_c]}{-c\cdot L_{gr}-\ln\{\cosh[c(L_{gr}-x_c)]\}+\ln\{\cosh[c\cdot x_c]\}}. \quad (11)$$

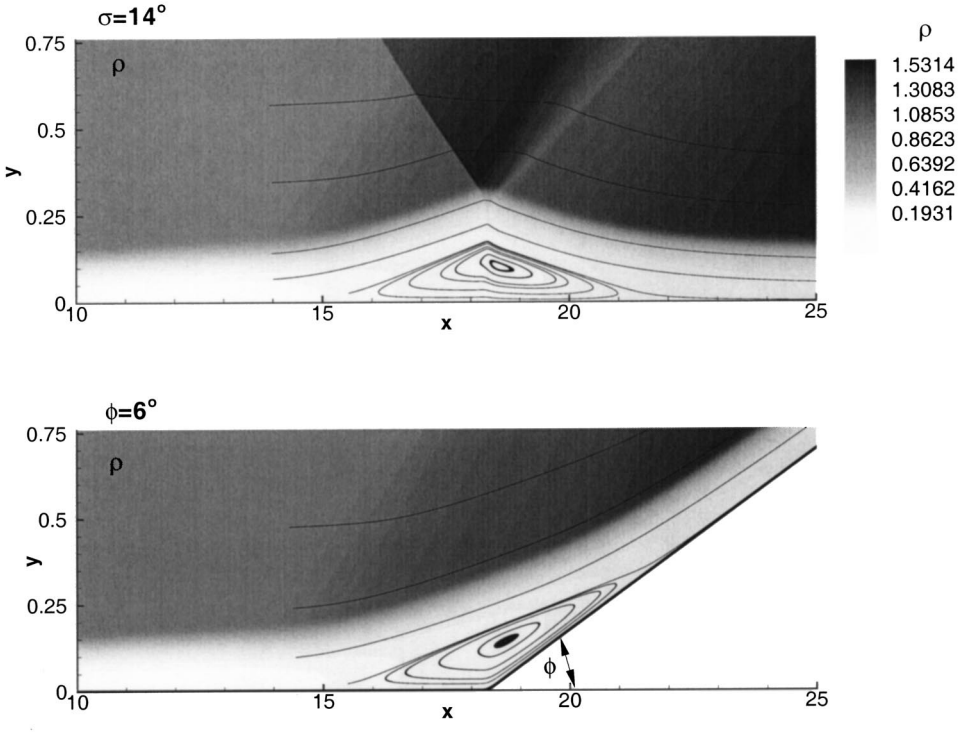

FIG. 2. Density fields for the case with impinging shock wave (upper figure) and the compression ramp (lower figure). Darker shadings indicate higher density. Note that figures are stretched in the y direction.

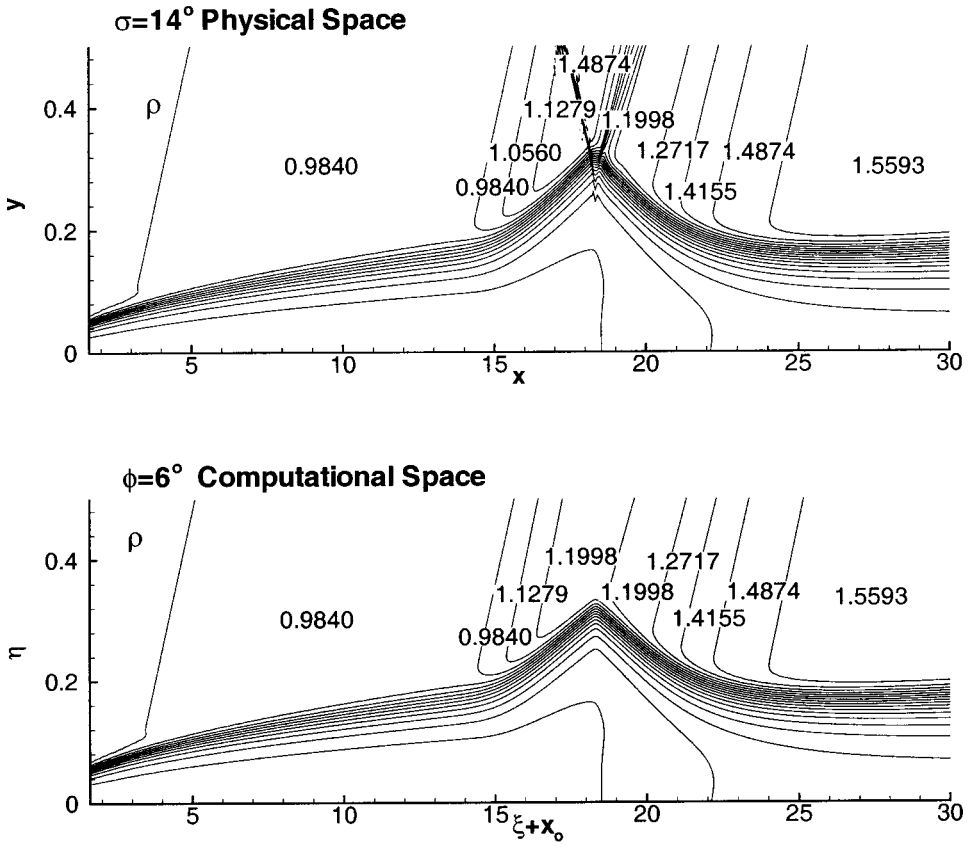

FIG. 3. Comparison of the density fields of the case with impinging shock in physical space to the compression corner in computational space.

L_{gr} is the length of the integration domain. In streamwise direction, we have

$$x = x_0 + \xi. \tag{12}$$

Equation (9) is solved both at the wall (y_w) and at the free-stream boundary (y_∞). Values are then interpolated between the upper and lower boundary for the whole field,

$$x_{(\xi,\eta)} = (1 - r_{(\eta)}) \cdot x_{w(\xi)} + r_{(\eta)} \cdot x_{\infty(\xi)}, \tag{13}$$

$$y_{(\xi,\eta)} = (1 - r_{(\eta)}) \cdot y_{w(\xi)} + r_{(\eta)} \cdot y_{\infty(\xi)}. \tag{14}$$

Interpolation in the wall-normal direction is calculated exponentially,

$$r_{(\eta)} = \frac{e^{(d \cdot \eta')} - 1}{e^d - 1}, \quad \eta' = \frac{\eta}{(M-1)\Delta\eta}. \tag{15}$$

The variable d specifies the magnitude of stretching in the wall-normal direction. Within the simulations presented here, an equidistant grid in both streamwise and wall-normal direction has been chosen ($d \to 0$), which is shown in Fig. 1. Therefore, $\Delta x = \Delta\xi$ and $\Delta y = \Delta\eta$. In our simulations, we use $\phi = 6°$, $x_c = 18.33$, at the wall $c_w = 10$, at $y = \infty$ $c_\infty = 0.5$, $d = 0.05$. Other relevant parameters of our simulations are given in Table I. $M/\Delta y$ and $N/\Delta x$ are the number of grid points/step sizes in the η and ξ direction, respectively.

III. RESULTS

A. Base flow

In the following, results for the compression ramp will be shown and compared to the flat-plate boundary layer with impinging shock. In both cases, the free stream Mach number is Ma=4.8, free-stream temperature $T_\infty = 55.4$ K and the wall temperature is held constant at $T_w = 270$ K. For the case with impinging shock on the flat plate the shock angle with respect to the wall is $\sigma = 14°$. For this case results were al-

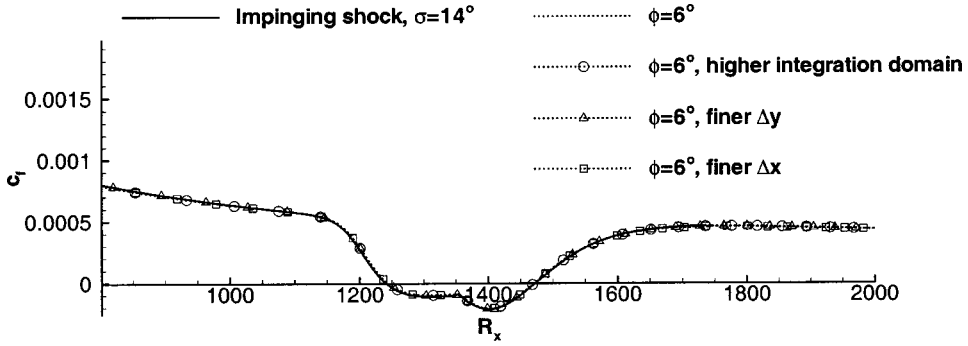

FIG. 4. Skin friction coefficient distribution c_f versus square root of local Reynolds number R_x. Comparison of case with impinging shock (solid line) and compression corner (dotted lines). Also given are results of grid-refinement/enlargement studies of the ramp flow (dotted lines with symbols).

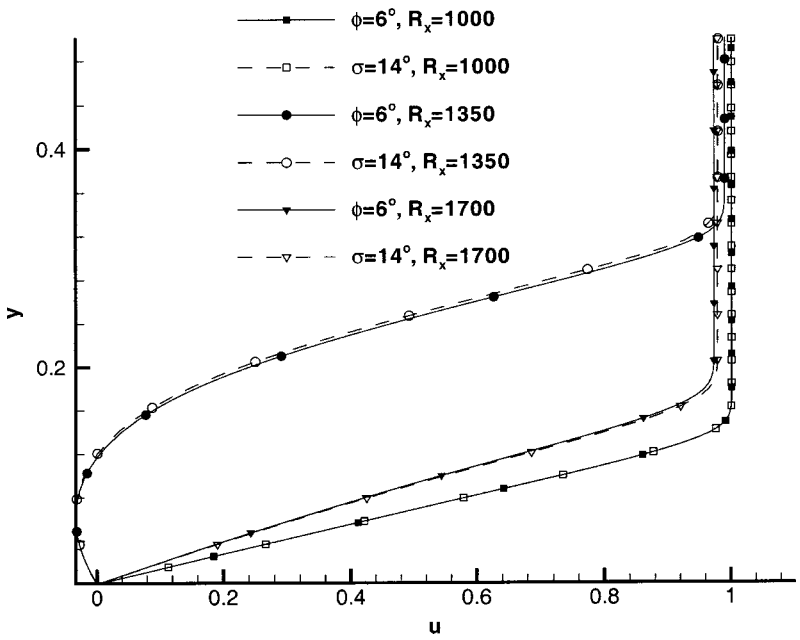

FIG. 5. Streamwise velocity components of base flow at three consecutive locations $R_x=1000$, $R_x=1350$, and $R_x=1700$. Here, the wall is at $y=0$.

ready published in Ref. 2. The ramp angle with respect to the horizontal direction is $\phi=6°$. As a first approximation for turbulent boundary layers a corner angle, half the angle of the impinging shock, gives a similar wall-pressure distribution in both cases, according to Ref. 3. The ramp angle of $\phi=6°$ was obtained by iteratively changing the wedge angle until maximum agreement with respect to the skin friction distribution. In Fig. 2 the density field for both cases is given. Also shown are selected streamlines, which visualize the flow in the free stream and in the boundary layer, where a separation bubble can be observed in both cases. It will be shown in the following, that the two flows are very similar.

When the flow field in the ramp case downstream of the corner is mapped on the flat plate, which means a rotation with its negative ramp angle the resulting flow field matches with the case with impinging shock. In Fig. 3 such a construction is given for the two density fields. As it can be seen, the two density fields look very similar except for the impinging shock and its reflection as an expansion wave at the sonic line, which is not present in the compression corner. The contour levels of both configurations agree quantitatively. For all other flow variables the results compare equally well.

We now take a closer look at the skin friction distributions, which are given in Fig. 4. It can be seen, that the skin friction of the compression ramp perfectly matches the skin friction of the case with impinging shock. Also shown in Fig. 4 are results of grid-refinement/enlargement studies (dotted lines with symbols, according to the legend). They prove the grid independency of our simulations. According results for the case with impinging shock can be found in Ref. 2.

In Fig. 5 u-velocity profiles at three locations R_x are compared for the ramp and the case with impinging shock. Profiles for $R_x=1000$ are identical. Near and at the wall the other velocity profiles agree very well with each other, even inside the separation bubble at $R_x=1350$. However, farther from the wall the profile at $R_x=1700$ has slightly lower velocity in the case of the impinging shock, while at $R_x=1350$ it is the opposite.

Figure 6 compares the wall-pressure distribution of both cases. As for the skin-friction distribution, the wall pressure is identical for both types of shock-boundary layer interaction.

Thus the base flow calculations presented here are in full agreement with free-interaction theory, which says, that the boundary layer behavior in shock-boundary layer interaction should be largely independent of its origin. This holds even quantitatively, as it can be seen in the present comparisons.

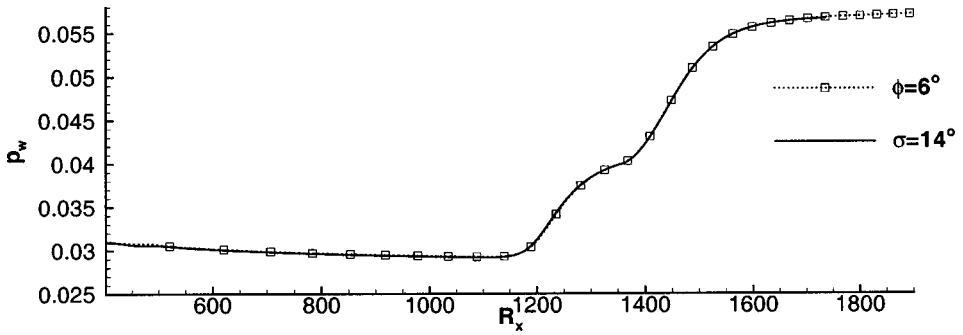

FIG. 6. Wall-pressure distribution versus square root of local Reynolds number R_x. Comparison of case with impinging shock (solid line) and compression corner (dotted lines with symbols).

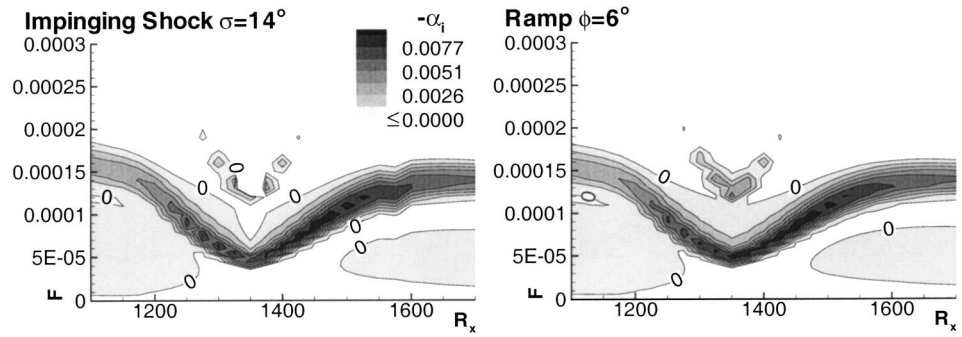

FIG. 7. Linear stability theory results. Disturbance frequency F versus local Reynolds number R_x. Darker shadings indicate larger amplification rates α_i. White represents negative/neutral amplification.

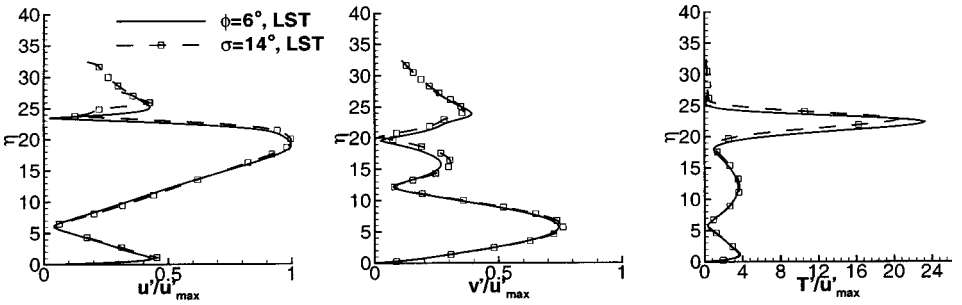

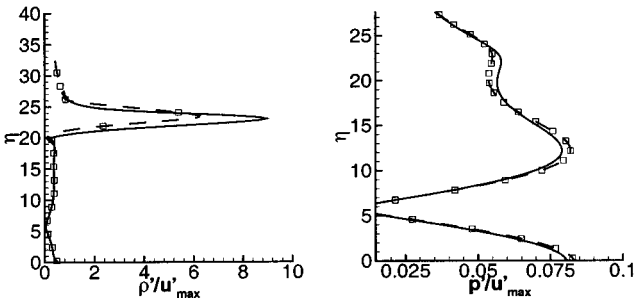

FIG. 8. Eigenfunctions of the primitive flow variables at $R_x = 1350$. Disturbance frequency $F = 0.0001$.

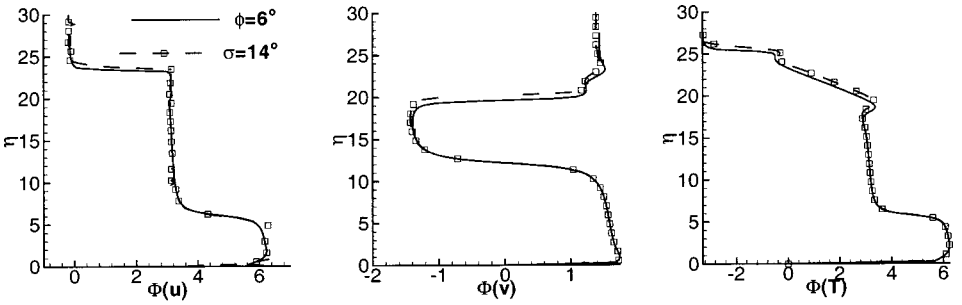

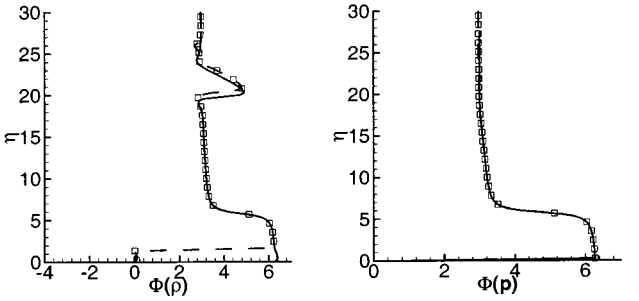

FIG. 9. Wall-normal phase distributions Φ of the primitive flow variables at $R_x = 1350$. Disturbance frequency $F = 0.0001$.

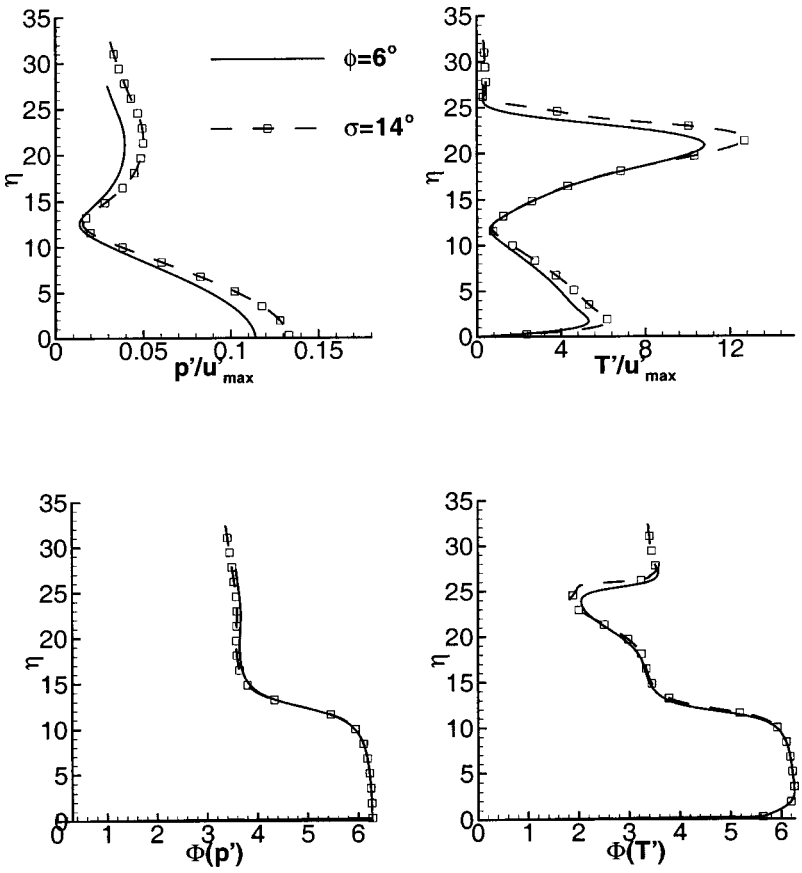

FIG. 10. Pressure, temperature eigenfunction and corresponding phase distribution at $R_x=1350$. Disturbance frequency $F=0.000\,05$.

B. Linear stability theory

We now compare compressible linear stability theory results obtained from investigations of the impinging shock with the compression ramp. Our linear stability theory results are based on the scheme developed by Mack.[4] Nonparallel effects are not taken into account here. The streamwise velocity and temperature profiles, which are used by linear stability theory, were extracted locally from the direct numerical simulations of the base flow as those shown in Fig. 5. Figure 7 compares the stability diagrams obtained by linear stability theory for the two cases. $F=(2\pi f^*L)/(u_\infty^*\,\mathrm{Re})$ is the disturbance frequency, darker shadings indicate larger amplification rates $\alpha_i=(-\partial\ln(A(x)/A_0))/\partial x$. As it can be seen, the two figures are virtually identical. Due to the influence of the shock, the first instability mode[4] is stabilized and the second mode[4] is destabilized and locally shifted to lower frequencies. New instabilities at higher frequencies are formed, near $R_x=1350$ and $F=0.000\,12$.

Some differences in Fig. 7 are present around $R_x\approx1350$, which is very close to the location of the corner and shock impingement on the boundary layer, respectively. To take a closer look at the disturbance behavior there, eigenfunctions and phase distributions at $R_x=1350$ are compared in Figs. 8, 9, 10, and 11 at three disturbance frequencies $F=0.0001$, $F=0.000\,05$, and $F=0.000\,12$, respectively. Here, $\eta=y\,\mathrm{Re}/R_x$ represents the wall normal coordinate. From the pressure eigenfunction and its corresponding phase distribution for $F=0.0001$ in Figs. 8 and 9, respectively, it can be seen that the stability regime at $R_x=1350$ with $F=0.0001$ belongs to a second mode, because the pressure eigenfunc-

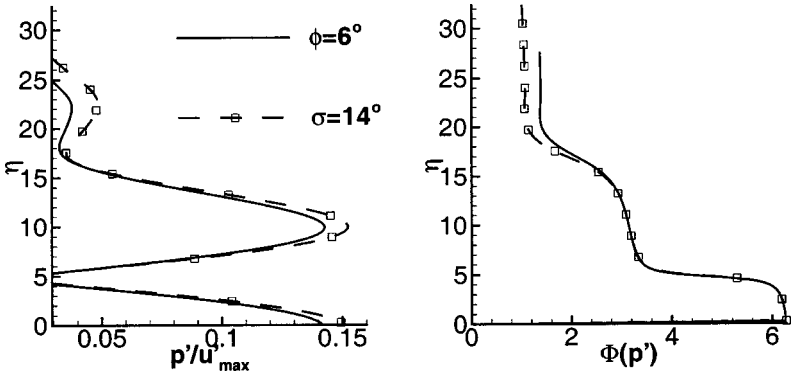

FIG. 11. Pressure eigenfunction and phase distribution at $R_x=1350$. Disturbance frequency $F=0.000\,12$.

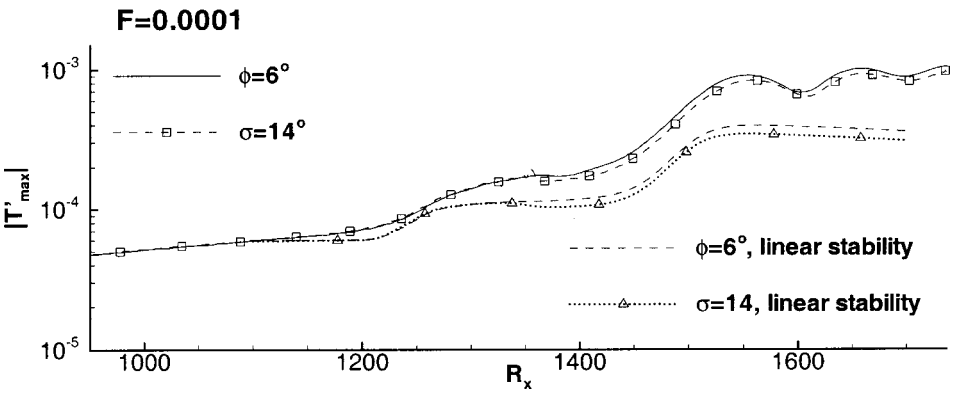

FIG. 12. Maximum temperature disturbance amplitudes of both direct numerical simulations and integrated amplification rates from linear stability theory versus R_x.

tion has one zero[4] in both cases. Eigenfunctions for the velocity components u and v and the pressure p quantitatively match. In the case with the compression ramp, the distributions for the temperature T and density ρ have larger absolute maxima compared to the case with impinging shock. However, the characteristics of the eigenfunctions are identical, as well.

The phase distributions in Fig. 9 all show very good quantitative agreement.

In both the cases with compression ramp and impinging shock we have a second mode-type disturbance at $R_x \approx 1350$ and $F=0.0001$. However, in the case with shock it is damped, while in the case of the compression corner it is amplified. The impinging shock seems to stabilize the flow in this regime.

Eigenfunctions and phase distributions for the pressure and temperature disturbances at $F=0.000\,05$ are given in Fig. 10. Qualitatively, the characteristics of the curves for the compression corner match the case with impinging shock. However, quantitative agreement is worse than for $F=0.0001$ in Figs. 8 and 9. The pressure eigenfunctions and phase distributions indicate, that $F=0.000\,05$ at $R_x=1350$ belongs to a second-mode instability like in the case with $F=0.0001$.

The newly formed disturbances, caused by the shock-boundary layer interaction at higher frequencies are of third-mode type. This can be inferred from the pressure eigenfunction, which has two zeros, and its corresponding phase distribution in Fig. 11. Higher mode instabilities, such as second and third modes, can be characterized as acoustic waves.[4] Differences between the ramp flow and the case with impinging shock are also larger than in Figs. 8 and 9, comparable to the case with $F=0.000\,05$ in Fig. 10.

C. Direct numerical simulations of small-amplitude disturbances

We now compare direct numerical simulations of small-amplitude disturbances. Because the two base flows are not identical in all aspects, i.e., there is no impinging shock and reflected expansion wave in the compression corner and curvatures of streamlines in physical space are different (see Fig. 2), differences between the two configurations might exist, which are not taken into account by linear stability theory. Therefore, a more detailed investigation with direct numerical simulation is appropriate. Figures 12 and 13 show the maximum temperature disturbance amplitudes and the wall pressure amplitudes versus the downstream coordinate, respectively. For the direct numerical simulations, they were obtained by a Fourier analysis of the flow variables over one disturbance period. The wall pressure and temperature were chosen here because of results obtained in Ref. 2. These two quantities have the largest and smallest nonparallel effects of all primitive flow variables in our simulations. Nonparallel effects highly influence the disturbance behavior, which was quantified in Ref. 2.

The differences between the amplitudes of the direct numerical simulation and linear stability, which can be seen in Figs. 12 and 13, were identified and quantified as an effect of nonparallelism for the case with impinging shock in Ref. 2. The strongest nonparallel effects appear in the maximum pressure disturbance, shown in Fig. 13. Disturbance behavior

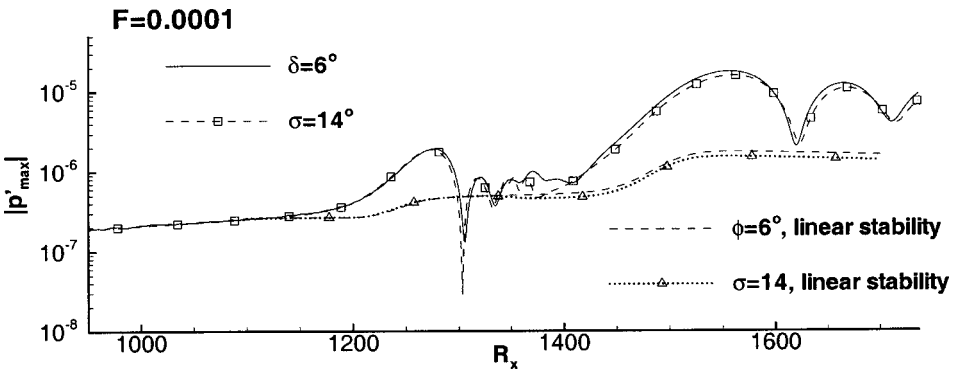

FIG. 13. Maximum pressure disturbance amplitudes of both direct numerical simulations and integrated amplification rates from linear stability theory versus R_x.

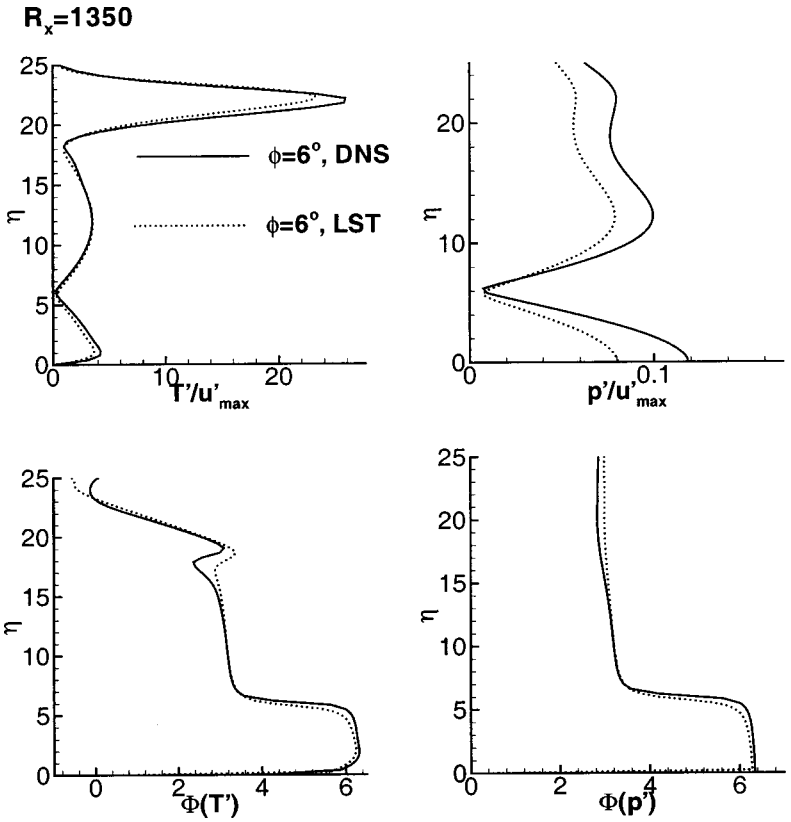

FIG. 14. Comparison of wall-normal amplitude and phase distributions for the ramp with corresponding linear stability results. Shown are temperature and pressure distributions. $R_x = 1350$, $F = 0.0001$.

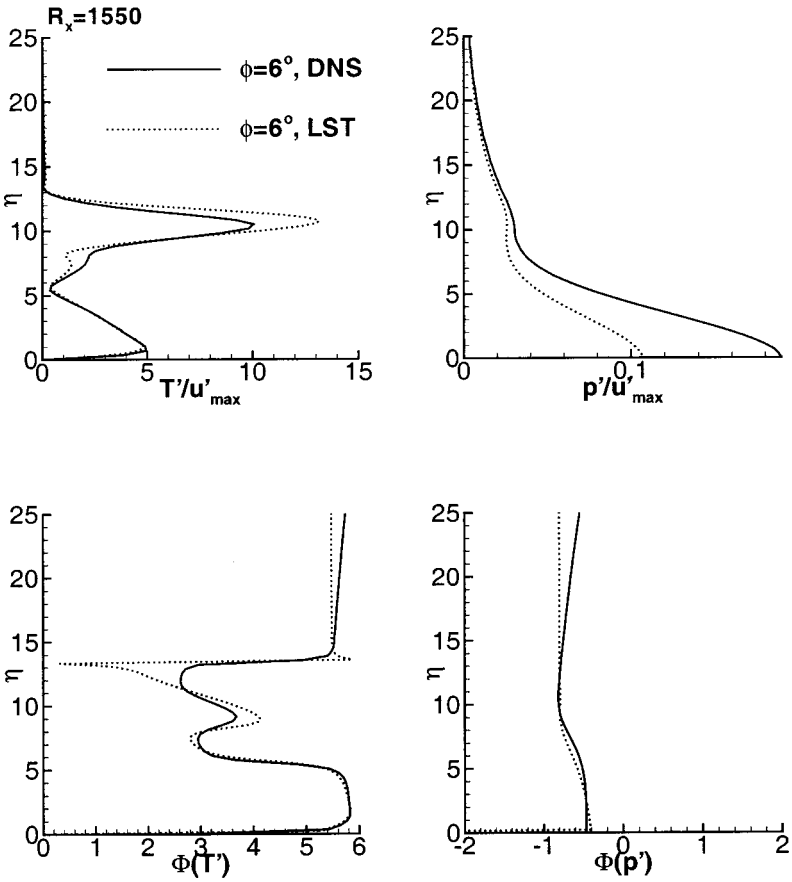

FIG. 15. Comparison of wall-normal amplitude and phase distributions for the ramp with corresponding linear stability results. Shown are temperature and pressure distributions. $R_x = 1550$, $F = 0.0001$.

of the case with impinging shock and the compression ramp look very similar for both the direct numerical simulation and linear stability. It is identical until shock impingement at $R_x \approx 1350$. Downstream of $R_x = 1350$ the amplitudes both for the maximum temperature amplitude and the wall pressure remain smaller in the case with impinging shock. As it was already discussed in the linear stability theory section of this paper, amplification rates in the case with impinging shock are slightly damped near shock impingement, which results in smaller disturbance amplitudes as it can be seen in Figs. 12 and 13 for both the direct numerical simulation and linear stability. However, compared to the nonparallel effects present in the DNS solutions such differences are marginal. For instance, the predicted amplification of linear stability theory between $R_x = 1100$ and $R_x = 1550$ would be ≈ 7. This is far less than the actually observed amplification of the temperature maxima and the wall-pressure fluctuations, which are ≈ 15 and ≈ 68, respectively. At $R_x = 1625$ the amplitude of the wall pressure is again very close to linear stability theory, because of considerable spatial variations.

For the temperature and the pressure with $F = 0.0001$ at $R_x = 1350$ wall-normal amplitude and phase distribution comparisons of direct numerical simulations of the ramp flow with corresponding linear stability results are given in Fig. 14. The same distributions for $R_x = 1550$, which is farther downstream and outside separation is shown in Fig. 15. For $R_x = 1350$ the agreement of the amplitude and phase distributions is significantly better compared to $R_x = 1550$. In the region upstream shock impingement, where disturbance amplitudes are identical, amplitude and phase distributions are identical as well and therefore not shown here.

As it can be seen, disturbance amplitudes for the temperature and phase distributions for both the temperature and the pressure show good agreement with linear stability theory. The pressure eigenfunction, however, has lower maxima than the corresponding amplitude distribution of the direct numerical simulation. This apparently is due to nonparallel effects. It is fully in line with the streamwise amplifications observed in Figs. 12 and 13, since the wall pressure becomes much larger compared to linear stability theory than the absolute temperature maximum. Results of the case with impinging shock are not repeated here, because they behave in a similar manner like in the linear stability section (see Figs. 8 and 9) regarding their agreement with the ramp case.

IV. CONCLUSION AND FUTURE POINTS OF INTEREST

It was shown, that the boundary layer under the influence of an impinging shock and along a compression ramp are practically identical. This holds for the base flow, linear stability theory, and direct numerical simulations of disturbance amplification with small-amplitude disturbances in two dimensions. Therefore, two-dimensional conclusions drawn in Ref. 2 can be applied to the compression ramp, too. These results are in accordance with earlier experimental observations and analytical concepts stating that the physics of such flows are not determined by the type of shock-boundary layer interaction, but rather determined by the flow-field properties at the onset of interaction. However, a different behavior between the compression ramp and the impinging shock might be expected in three dimensions and the nonlinear cases. In the ramp-flow streamline curvature is different compared to the impinging shock. Three-dimensional and nonlinear simulations could shed some more light on the issue whether two-dimensional higher acoustic modes or three-dimensional waves are the main route of transition in such flows. Such simulations should therefore be included in further studies.

ACKNOWLEDGMENT

The authors would like to thank the *Deutsche Forschungsgemeinschaft* for supporting this research within *Sonderforschungsbereich 259* at the University of Stuttgart and for computing time provided by the High Performance Computing Center in Stuttgart (HLRS).

[1] J. Délery and J. G. Marvin, "Shock-wave boundary layer interactions," AGARDograph 280 (1986).
[2] A. Pagella, U. Rist, and S. Wagner, "Numerical investigations of small-amplitude disturbances in a boundary layer with impinging shock wave at Ma=4.8," Phys. Fluids **14**, 2088 (2002).
[3] D. Knight, H. Yan, A. G. Panaras, and A. Zheltovodov, "Advances in CFD prediction of shock wave turbulent boundary layer interactions," Prog. Aerosp. Sci. **39**, 121 (2003).
[4] L. Mack, "Boundary layer stability theory," Jet Propulsion Laboratory, Pasadena, Technical Report 900-277 (1969).
[5] W. Eißler and H. Bestek, "Direct numerical simulation of transition in Mach 4.8 boundary layers at flight conditions," in *Engineering Turbulence Modelling and Experiments*, edited by W. Rodi and G. Bergeles (Elsevier, New York, 1996), Vol. 3, pp. 611–620.
[6] J. Anderson, Jr., *Computational Fluid Dynamics* (McGraw-Hill International, New York, 1995), pp. 168–215.
[7] S. Lele, "Compact finite difference schemes with spectral-like resolution," J. Comput. Phys. **103**, 16 (1992).
[8] W. Eißler and H. Bestek, "Spatial numerical simulations of linear and weakly nonlinear wave instabilities in supersonic boundary layers," Theor. Comput. Fluid Dyn. **8**, 219 (1996).
[9] N. Adams, "Direct simulation of the turbulent boundary layer along a compression ramp at $M=3$ and $\mathrm{Re}_\theta=1685$," J. Fluid Mech. **420**, 47 (2000).